PCCP

ROYAL SOCIETY OF CHEMISTRY

PAPER

View Article Online
View Journal | View Issue

Cite this: *Phys. Chem. Chem. Phys.*, 2020, **22**, 27829

Role of hemibonding in the structure and ultraviolet spectroscopy of the aqueous hydroxyl radical†

Bhaskar Rana and John M. Herbert *

The presence of a hemibond in the local solvation structure of the aqueous hydroxyl radical has long been debated, as its appearance in *ab initio* simulations based on density functional theory is sensitive to self-interaction error (favoring a two-center, three-electron hemibond) but also to finite-size effects. Simulations reported here use a mixed quantum mechanics/molecular mechanics (QM/MM) framework in a very large periodic simulation cell, in order to avoid finite-size artifacts and to facilitate testing of various density functionals, in order to probe the effects of delocalization error. The preponderance of hemibonded structures predicted by generalized gradient approximations persists in simulations using the hybrid functionals B3LYP and PBE0, but is reduced to a minor population if the fraction of exact exchange is increased to 50%. The hemibonded population is also small in simulations employing the long-range corrected functional LRC-ωPBE. Electronic spectra are computed using time-dependent density functional theory, and from these calculations emerges a consensus picture in which hemibonded configurations play an outsized role in the absorption spectrum, even when present as a minority species. An intense $1b_2(H_2O) \rightarrow 2p\pi(^{\bullet}OH)$ charge-transfer transition in hemibonded configurations of the radical proves to be responsible for an absorption feature at 230 nm that is strongly shifted with respect to the gas-phase absorption at 307 nm, but this intense feature is substantially diminished in aqueous geometries where the hemibond is absent. Although not yet sufficient to quantitatively establish the population of hemibonded $^{\bullet}$OH(aq), these simulations do suggest that its presence is revealed by the strongly shifted ultraviolet absorption spectrum of the aqueous radical.

Received 4th October 2020,
Accepted 11th November 2020

DOI: 10.1039/d0cp05216g

rsc.li/pccp

1 Introduction

The hydrated hydroxyl radical plays a significant role in biological, atmospheric, and industrial processes.[1–5] The solvation structure of $^{\bullet}$OH(aq) has long been studied *via ab initio* molecular dynamics.[6–22] Its diffusion constant[23,24] is nearly identical to water's self-diffusion constant (see Table 1),[25] and is therefore much slower than the Grotuß-assisted diffusion of either H^+(aq) or OH^-(aq),[26–28] or the librationally-assisted diffusion of e^-(aq).[29] What has proved most contentious, however, is the putative existence of a two-center, three-electron "hemibond" in the first solvation shell of $^{\bullet}$OH(aq). An example of such a structure is shown in Fig. 1 for the complex of $^{\bullet}$OH with a single water molecule.[30] The hemibonded motif is available due to a favorable overlap between the singly-occupied 2pπ molecular orbital (MO) of the radical and the frontier $1b_2$ lone pair of a neighboring water molecule.[15] Sulfur–sulfur hemibonds have convincingly been identified in gas-phase systems including $(H_2S)_n^+$,[31–33] $[(CH_3)_2S]_2^+$,[34] and $(CH_3SH)_2^+$,[35] and have long been discussed in the context of aqueous pulse radiolysis experiments,[36–39] where they might be born from sulfur-centered radical cations that dimerize with a molecule of the parent species. Unequivocal identification of hemibonding in $^{\bullet}$OH(aq) has proven elusive, however.

Table 1 Diffusion constants for some aqueous species at 25 °C

Species	D (Å^2 ps^{-1})	Ref.
H^+	0.93	28
$H^{\bullet}$	0.7–0.8	23
OH^-	0.53	28
e^-	0.48–0.49	23
H_2O	0.23	25
$HO^{\bullet}$	0.21–0.23	23
Cl^-	0.20	28

Department of Chemistry & Biochemistry, The Ohio State University, Columbus, OH, USA. E-mail: herbert@chemistry.ohio-state.edu

† Electronic supplementary information (ESI) available: Additional calculations and analysis. See DOI: 10.1039/d0cp05216g

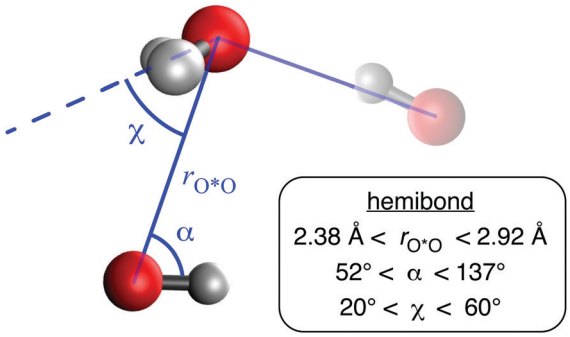

Fig. 1 Schematic view of the hemibonded $H_2O\cdots{}^{\bullet}OH$ complex (opaque models) along with a translucent hydroxyl radical in a hydrogen-bonded orientation. Quantitative suggestions for the geometrical parameters that define the hemibonded structure are taken from ref. 30.

Whereas definitive experimental evidence is lacking, there is no shortage of *ab initio* molecular dynamics (*ai*MD) studies that have identified the presence of hemibonding in $^{\bullet}OH$(aq).[6–8,12–16] Looming over these studies, however, is the specter of self-interaction error (SIE) in density functional theory (DFT).[40] Over-delocalization of radical centers is a known artifact of SIE,[40–42] affecting such diverse systems as polarons in TiO_2,[43] hole defects in silica,[44–46] cation radicals including ionized water clusters[47,48] and $(guanine)_2^+$,[49] anionic water clusters,[50–52] radical-molecule complexes,[53,54] and ion-radical complexes such as $HOCl^-$.[55,56] In the latter case, SIE overstabilizes the hemibonded configuration $HO^{\bullet}\cdots Cl^-$, relative to the hydrogen-bonded geometry $^{\bullet}OH\cdots Cl^-$.[55,56] Therefore when hemibonded configurations of $^{\bullet}OH$(aq) were observed in early *ai*MD simulations of $^{\bullet}OH$(aq), it was immediately considered that these might be artifacts of SIE.[6–8] More recently, however, this point of view has been challenged by Kusalik and co-workers,[12–15] as discussed below.

A summary of previous *ai*MD simulations of $^{\bullet}OH$(aq) is presented in Table 2. In some of these studies, the presence of a hemibonded solvation motif manifests as a distinct feature in the $O^*\cdots O$ radial distribution function (RDF), where O^* denotes the oxygen atom of the radical. This feature, if present, appears around $r_{O^*O} \approx 2.3-2.4$ Å. Vassilev *et al.*[6,7] and Khalack *et al.*[9] performed *ai*MD simulations using the BLYP functional,[57,58] placing 31 waters (along with $^{\bullet}OH$) in the simulation cell. A peak in the aforementioned RDF around $r_{O^*O} \approx 2.3$ Å was attributed to an average coordination structure that is hemibonded, though it was acknowledged at the time that this could be an artifact of SIE.[6] Recognizing this, VandeVondele and Sprik[8] added an empirically-parameterized self-interaction correction (SIC) to BLYP, and observed that the hemibonded structures disappeared in simulations that employed this BLYP-SIC functional. For a time, this study cemented the conventional wisdom that the hemibonded structure is an artifact of SIE.

However, this interpretation was subsequently challenged by Codorniu-Hernández and Kusalik.[12–15] These authors do observe a hemibonded structure when $^{\bullet}OH$(aq) is simulated in a periodic cell with $N = 31$ water molecules, using either the BLYP or HCTH/120[59] functionals with no SIC.[12] When the periodic cell is expanded to $^{\bullet}OH(H_2O)_{63}$, however, the hemibonded configurations disappear. Later, these authors computed potentials of mean force along the $O^*\cdots O$ coordinate using various functionals (in the larger simulation cell), and demonstrated the existence of the hemibond as an alternative structure, with a barrier of 2–3 kcal mol^{-1} separating it from the hydrogen-bonded structure.[15] Although Codorniu-Hernández *et al.*[12,15] attribute the hemibonded solvation motif to an artifact of finite simulation size, this does not entirely explain its disappearance, in smaller simulations using $N = 31$ water molecules, when a SIC is added to BLYP.[8] In the larger ($N = 63$) simulation cell, *ai*MD simulations suggest that the hemibonded structure is absent whether a SIC is applied or not.[20]

The phenomenon of SIE is often associated with semilocal functionals developed within the generalized gradient approximation (GGA), and hybrid functionals that introduce a fraction of "exact" (Hartree–Fock) exchange are viewed as an antidote to this problem. Especially in the condensed-matter simulation community, we observe a tendency to view hybrid functionals

Table 2 Summary of previous *ai*MD studies of $^{\bullet}OH$(aq), indicating whether or not the authors report a hemibonded solvation structure

Reference	Unit cell	Functional	Hemibond?	T (K)
Khalack and Lyubartsev[9] (2004)	$^{\bullet}OH(H_2O)_{31}$	BLYP	✓	310
Vassilev *et al.*[6] (2005)	$^{\bullet}OH(H_2O)_{31}$	BLYP	✓	300
VandeVondele and Sprik[8] (2005)	$^{\bullet}OH(H_2O)_{31}$	BLYP-SIC	✗	350
Codorniu-Hernandez and Kusalik[12] (2011)	$^{\bullet}OH(H_2O)_{31}$	BLYP	✓	310
	$^{\bullet}OH(H_2O)_{31}$	HCTH/120	✓	310
	$^{\bullet}OH(H_2O)_{63}$	BLYP	✗	310
	$^{\bullet}OH(H_2O)_{63}$	HCTH/120	✗	310
Genova *et al.*[20] (2016)	$^{\bullet}OH(H_2O)_{63}$	revAPBEK	✗	340
	$^{\bullet}OH(H_2O)_{63}$	revAPBEK-SIC	✗	340
von Rudorff *et al.*[16] (2017)	$^{\bullet}OH(H_2O)_{31}$	BLYP+D3	✓	—
	$^{\bullet}OH(H_2O)_{31}$	HSE06+D3	✗	—
Apostolidou[21] (2019)	$^{\bullet}OH(H_2O)_{31}$	B3LYP+D3	✗	370
	$^{\bullet}OH(H_2O)_{31}$	PBE0+D3	✗	370
	$^{\bullet}OH(H_2O)_{31}$	HSE03+D3	✗	370

such as PBE0,[60] with 25% exact exchange, as being largely free of the effects of SIE, although this is not true and does not stand up to close scrutiny.[61,62] Often, hybrids containing $\gtrsim$50% exact exchange are needed to substantially eliminate SIEs in barrier heights,[63,64] with deleterious effects on other predicted properties.[63] It is true, however, that the (de)localization of an unpaired spin may correlate with the fraction of exact exchange.[44–46,49–51] Application of a SIC to the singly-occupied MO (SOMO) also serves to localize the unpaired spin.[49,52]

Hybrid-functional *ai*MD simulations have recently been brought to bear on $^{\bullet}$OH(aq) by Apostolidou,[21] using the smaller (N = 31) simulation cell in conjunction with the B3LYP,[58,65] PBE0,[60] and HSE03[66] functionals. (Unlike other simulations mentioned above, these ones also employed an empirical dispersion correction, +D3.[67]) In these simulations, the average structure is hydrogen-bonded rather than hemibonded, despite the use of a smaller cell, suggesting perhaps a delicate interplay between simulation size, SIE, and the structure that is obtained. In the present work, we will use a quantum mechanics/molecular mechanics (QM/MM) framework that facilitates the use of a very large periodic cell, in order to avoid any potential artifacts due to finite-size effects.

Apart from these questions regarding the structure of $^{\bullet}$OH(aq), there have been separate experimental and theoretical efforts to assign the peak in the ultraviolet (UV) absorption spectrum of this species, and hemibonded configurations have been suggested to play a role in its very intense absorption.[30] In the gas phase, $^{\bullet}$OH absorbs at 307 nm (4.04 eV),[68,69] corresponding to the $\tilde{A}^2\Sigma^+(\sigma_{lp}^2\sigma_b^1\pi^4) \leftarrow \tilde{X}^2\Pi(\sigma_{lp}^2\sigma_b^2\pi^3)$ transition.[70] The absorption maximum of $^{\bullet}$OH(aq), however, is shifted to 230 nm (5.4 eV),[71–74] much too large to be a non-specific medium effect (*e.g.*, from the dielectric environment),[70,73] although this explanation has been suggested.[75] More recently, the temperature dependence of the $^{\bullet}$OH(aq) absorption spectrum was measured,[76] showing that a weaker band at 310 nm grows in intensity at higher temperature while the stronger band at 230 nm diminishes. The transition at 230 nm was ascribed to a charge-transfer (CT) transition from a hydrogen-bonded water molecule to the radical, whereas the band near 310 nm was assigned to the localized transition on the radical itself, analogous to the gas-phase transition at 307 nm.[76]

Theoretical studies of the spectroscopy of the hydrated $^{\bullet}$OH radical have so far been limited to gas-phase cluster studies.[30,70,77–79] Excited states of the binary $^{\bullet}$OH(H_2O) complex have been reported using equation-of-motion coupled-cluster (EOM-CC) calculations including connected triples (EOM-CCSDT),[30,70] and small clusters $^{\bullet}$OH(H_2O)$_n$ have also been studied using EOM-CCSD, up to n = 7.[77,79] Excited states of a single $^{\bullet}$OH(H_2O)$_{16}$ cluster have been reported using time-dependent (TD-)DFT.[77] Each of these studies confirms the existence of a $H_2O \rightarrow {}^{\bullet}OH$ transition whose intensity is sensitive to orbital overlap,[77] and which is suggested to be responsible for the aqueous-phase absorption at 230 nm. Chipman[30] specifically ascribes the intense CT transition to hemibonded configurations of the radical, which he suggests might be rare in the liquid but which nevertheless dominate the absorption spectrum of $^{\bullet}$OH(aq) by virtue of a very large oscillator strength. So far, however, there are no condensed-phase simulations of the absorption spectrum that might tie this observable to the aforementioned structural ambiguities surrounding the hemibonded coordination motif. Such studies are reported here for the first time.

We report QM/MM simulations of $^{\bullet}$OH(aq) using a large, periodic simulation cell and various density functionals ranging from BLYP to hybrids (B3LYP and PBE0) and finally a range-separated hybrid, LRC-ωPBE.[80] Hemibonded configurations appear in each of these simulations, to a greater or lesser extent that we will analyze. Ensemble-averaged absorption spectra are then computed using TD-DFT in an effort to test the aforementioned hypothesis, that hemibonded configurations play an outsized role in the absorption spectrum of $^{\bullet}$OH(aq).

2 Computational details

2.1 QM/MM simulations

All QM/MM simulations were performed using Q-Chem,[81] v. 5.1. The QM region was described using either B3LYP, PBE0, or LRC-ωPBE in conjunction with the 6-31G* basis set and the D3 dispersion correction.[67] A range-separation parameter ω = 0.380 a_0^{-1} is used for LRC-ωPBE, which is very close to the "tuned" values that are selected below based on the ionization energy theorem.[82] Trajectories were initiated from an equilibrated liquid water trajectory by removing one hydrogen atom near the center of the simulation cell and then performing energy minimization prior to MD simulations.

Periodic boundary conditions were applied using a cubic box of length L = 31.342 Å, containing 1023 water molecules and one hydroxyl radical. This affords a density of 0.997 g cm^{-3}, matching liquid water's density at T = 300 K. The QM region was selected to match the smaller simulation cells used in previous *ai*MD simulations (see Table 2), taking the N = 31 water molecules that lie within a radius of 5.8 Å of the radical. The remaining water molecules are described using the TIP3P force field.[83] All simulations were performed under constant *NVT* conditions using a Nosé–Hoover thermostat[84] set to T = 300 K. Initial velocities were sampled from a Maxwell–Boltzmann velocity distribution at T = 300 K and then propagated using the velocity Verlet algorithm with a time step of 42 a.u. (= 1.016 fs). The self-consistent field (SCF) guess was regenerated at each time step in order to avoid energy drift caused by violation of time-reversal symmetry.[85] The SCF convergence threshold was set to $\tau_{SCF} = 10^{-6}E_h$, sufficient for energy conservation.[85]

Periodic boundary conditions were implemented using the QM/MM-Ewald technique that we have previously described[86,87] and applied to systems such as e^-(aq).[87,88] Periodic images of the QM atoms are represented using ChElPG charges,[89–91] derived from the QM electrostatic potential. For efficiency, we use an implementation of the ChElPG algorithm based on atom-centered Lebedev grids,[86] with 50 angular points per

radial shell. These shells begin at the atomic van der Waals radius of each atom and extend for another 5 Å, in 0.3 Å intervals. Separate Ewald splitting parameters are used to describe the MM/MM and QM/MM interactions. Following previous work,[86,87] the Ewald splitting parameter η_{MM} for the MM/MM interactions is taken to be $\eta_{MM} = 2C/L$ where

$$C = [-\ln(\tau_{SCF}/E_h)]^{1/2}. \quad (1)$$

With $\tau_{SCF} = 10^{-6}E_h$, this affords $\eta_{MM} = 0.237$ Å^{-1}. An optimal splitting parameter η_{QM} for the QM/MM interactions is estimated using the equation[86,87]

$$\frac{2CL^3\eta_{QM}^3}{\pi^{3/2}} + \frac{L^2\eta_{QM}^2}{\pi^{1/2}} - L\eta_{QM} - 2C = 0, \quad (2)$$

from which we obtain $\eta_{QM} = 0.0566$ Å^{-1}.

We simulate 5 ps trajectories but exclude from the analysis the first 0.5 ps, during which the temperature equilibrates (see Fig. S1, ESI†). We also exclude any portion of the trajectory where the radical approaches the QM/MM boundary, or where there is significant penetration of MM water molecules into the QM region. In principle, this could be avoided through the use of adaptive-partitioning QM/MM boundary conditions,[92] but would greatly increase both the complexity and the cost of the simulations. Alternatively a confining potential could be added to the QM/MM interface,[93] at the risk of introducing artifacts in the local solvation structure. We have chosen not to apply these techniques, which limits our trajectories to 4–5 ps in duration.

2.2 Absorption spectrum

Absorption spectra were computed by extracting 80–100 snapshots from each trajectory, separated by 50 fs intervals. From each snapshot, a TD-DFT/MM calculation was prepared in the following way. First, a 3 × 3 supercell was formed from the periodic simulation cell, and from that supercell a QM region extending to a radius of 5.5 Å around the •OH was selected, containing 30–34 water molecules. The remaining atoms in the supercell were represented by MM point charges. TD-DFT calculations were performed within the Tamm–Dancoff approximation.[94]

At each snapshot, we first compute a vertical excitation spectrum consisting of the lowest 15 excited states, whose oscillator strengths are given by

$$f_{0n} = \left(\frac{2m_e\omega_{0n}}{3\hbar}\right)\sum_{\kappa=x,y,z}|\langle\Psi_0|\hat{\kappa}|\Psi_n\rangle|^2 \quad (3)$$

where $\omega_{0n} = (E_n - E_0)/\hbar$. We then apply Lorentzian broadening (with a width of 0.2 eV) to each vertical transition, and weight each transition by its oscillator strength f_{0n}. Finally, an ensemble-averaged spectrum is obtained by averaging these individual broadened spectra.

Four different functionals are tested for the TD-DFT calculations, in conjunction with the 6-31++G* basis set. These include the BH&HLYP functional, which Chipman found to afford satisfactory agreement with EOM-CCSDT benchmarks for the •OH(H_2O) complex,[70] and also CAM-B3LYP.[95] Anticipating an important CT transition, we have used two long-range corrected (LRC) functionals, namely, LRC-ωPBE[80] and LRC-μBLYP,[96,97] each of which exhibits proper asymptotic behavior for a well-separated electron and hole. Range-separation parameters (ω or μ) were tuned separately for each of the trajectories, using the "optimal tuning" (OT) procedure[82] in an ensemble-averaged way. Specifically, we use 8–10 well-separated snapshots to find the value of ω that best satisfies the condition

$$IE(\omega) = -\varepsilon_{SOMO}(\omega) \quad (4)$$

in an average way for all snapshots. (The quantity IE in this equation denotes the ionization energy computed by a ΔSCF procedure, and ε_{SOMO} is the Kohn–Sham eigenvalue for the SOMO.) These tuned functionals are denoted OT-LRC-ωPBE and OT-LRC-μBLYP. For the prediction of CT energetics, the OT procedure can inoculate the results against some of the functional-to-functional variations that would otherwise be observed when off-the-shelf functionals are used to examine excited states with CT character.[98]

3 Structure of •OH(aq)

We will divide the discussion of our results into two parts. In this section, we discuss structural aspects of the aqueous hydroxyl radical and compare to previous work. The absorption spectroscopy, which is carried out for the aqueous phase for the first time, is discussed in Section 4, where we connect the spectroscopy back to the structural motifs (hemibond *versus* hydrogen bond) that are discussed here. Throughout this discussion, the atoms of the hydroxyl radical are indicated as O* and H*.

3.1 Radial distribution functions

Fig. 2 compares the RDFs $g(r_{O^*O})$ from the various simulations. These are computed using a bin width of 0.05 Å using the snapshots from the post-equilibration period. (See Fig. S5–S7, ESI† for convergence tests, using both additional trajectories as well as different subsets of the data, demonstrating that the

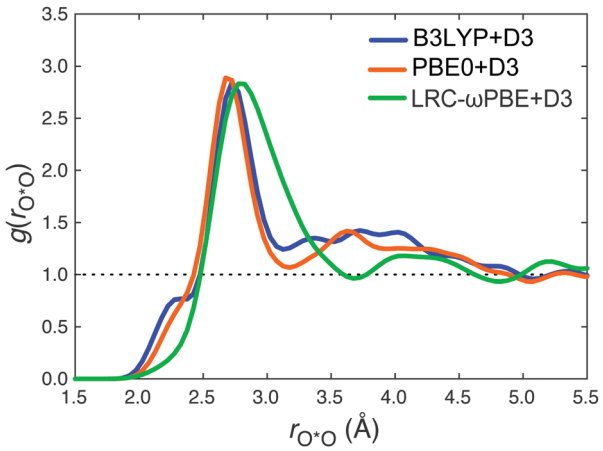

Fig. 2 Comparison of RDFs $g(r_{O^*O})$ for •OH(aq), where O* indicates the hydroxyl oxygen. Results were obtained from QM/MM simulations using three different density functionals.

first solvation shell in these RDFs is converged with respect to sampling.) As discussed in previous work,[6,8,9,12,16,20,21] the quantity $g(r_{O^{\star}O})$ plays an important role in identifying the presence or absence of a hemibonded configuration, with a sharp peak around $r_{O^{\star}O} \approx 2.3$–$2.4$ Å indicating that the hemibond exists as the predominant structure rather than as a rare event or fluctuation.[8] In the B3LYP+D3 and PBE0+D3 simulations reported here, this peak appears to be present but is not nearly so pronounced as it is in previous studies that report a hemibonded structure.[8,12] Especially in the case of our PBE0 simulations, the hemibonded feature appears as a shoulder that is partially subsumed into a larger peak centered at $r_{O^{\star}O} \approx 2.6$–$2.7$ Å that represents the ever-present $HO^{\bullet}\cdots H_2O$ hydrogen bonds.

In the LRC-ωPBE+D3 simulation, however, there is no evidence for a distinct feature in the RDF that might correspond to a hemibond. It is possible that it could be obscured by the hydrogen-bonding peak, which is much broader in the case of LRC-ωPBE+D3 than it is for the other two functionals, indicating a less structured liquid. Based on calculations for binary $HO^{\bullet}\cdots H_2O$ complexes, Chipman[30] has suggested that the hemibond could be characterized by a broad distribution of $O^{\star}\cdots O$ distances, roughly $r_{O^{\star}O} \approx 2.38$–$2.92$ Å as indicated in Fig. 1. If a hemibonded configuration does exist in the LRC-ωPBE+D3 simulations but is characterized by a slightly larger value of $r_{O^{\star}O}$ than in other simulations, it is possible that this feature could hide underneath the larger distribution of hydrogen-bonded $O^{\star}\cdots O$ distances. Below, we will introduce definitions of the hemibond that are based not just on geometrical structure but also on examination of the spin density, which suggest that hemibonded configurations do exist in the LRC-ωPBE+D3 simulation although they are a minority population.

To investigate the extent to which the fraction of exact exchange plays a role in the presence or absence of this hemibonded shoulder in $g(r_{O^{\star}O})$, we have also run a few shorter trajectories with the BLYP+D3 and BH&HLYP+D3 functionals, and with dispersion-corrected Hartree–Fock theory (HF+D3). The resulting $O^{\star}\cdots O$ RDFs are provided in Fig. S3 of the ESI.† For BLYP+D3, the hemibonded peak at $r_{O^{\star}O} \approx 2.3$ Å is much more pronounced than it is even in the B3LYP+D3 simulation (Fig. S3a, ESI†) and is consistent with the BLYP results reported by VandeVondele and Sprik, prior to application of the SIC.[8] In contrast, simulations with BH&HLYP+D3 (with 50% exact exchange) and HF+D3 afford RDFs that are very similar to those obtained with LRC-ωPBE+D3; see Fig. S3b (ESI†). Together, these comparisons hint that the hemibonded feature observed in our B3LYP+D3 and PBE0+D3 simulations may stem from SIE, despite the fact that these are hybrid functionals.

It is also worth noting that our B3LYP+D3 and PBE0+D3 results disagree with recent *ai*MD simulations that were reported using the same functionals,[21] in which no feature at small $r_{O^{\star}O}$ is observed. Simulations reported in ref. 21 used a periodic cell containing $N = 31$ water molecules, and may therefore be subject to finite-size artifacts. If so, then it is notable that such artifacts induce the formation of a hemibonded structure when GGA functionals are employed (as documented in ref. 12), but disrupt the hemibond when hybrid functionals are employed. We have no further explanation for these discrepancies except to note that it is clear from our own simulations (Fig. 2) that the distribution of hydrogen bond lengths is sensitive to the choice of functional and that depending on the details of this distribution, the hydrogen-bonding peak in $g(r_{O^{\star}O})$ may obscure the hemibonded peak, partially if not fully. Indeed, we will document below that hemibonded structures are present even in the LRC-ωPBE+D3 simulations that we report (although they are a minority population), despite the absence of any distinct feature in $g(r_{O^{\star}O})$ that would indicate their presence.

The comparison among the oxygen–hydrogen RDFs is also important, specifically to characterize the strength of $^{\bullet}OH$ as a hydrogen-bond donor or acceptor. Fig. 3 compares the three different types of oxygen–hydrogen RDF: $H\cdots O^{\star}$, $H^{\star}\cdots O$, and $H\cdots O$. (The PBE0+D3 results are similar to the B3LYP+D3 results and can be found in Fig. S4, ESI.†) As compared to the $H\cdots O$ distribution, which measures the distribution of water–water hydrogen bond lengths, the first peak in the $H^{\star}\cdots O$ distribution appears at a shorter distance, suggesting that the radical is a better hydrogen-bond donor as compared to a water molecule. However, the strength of $^{\bullet}OH$ as a

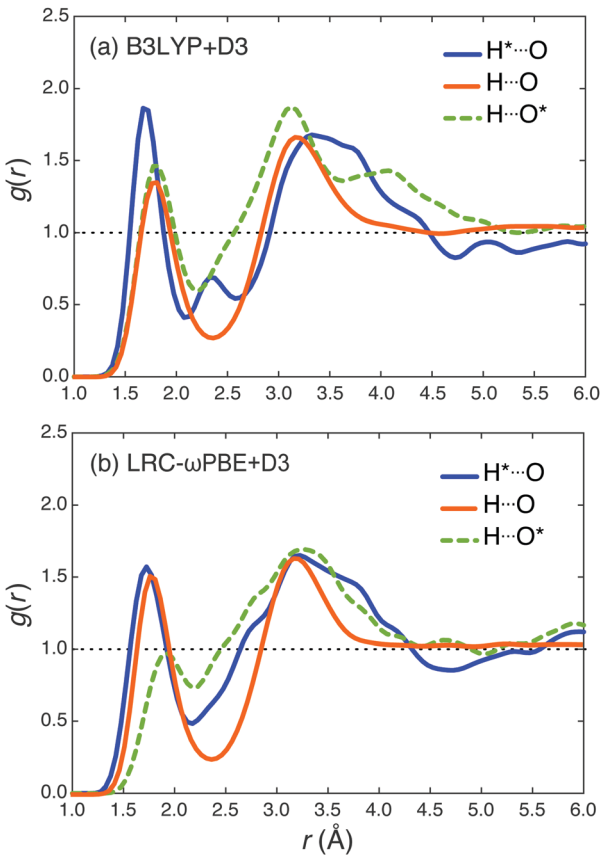

Fig. 3 Comparison of different oxygen–hydrogen RDFs obtained from (a) B3LYP+D3 *versus* (b) LRC-ωPBE+D3 simulations. Covalent bonds have been excluded from the averaging so that $g(r_{OH})$ represents the RDF for hydrogen bonds only.

hydrogen-bond acceptor differs in the two simulations shown in Fig. 3, as becomes apparent in comparing the H···O* and H···O distributions. According to B3LYP+D3 results, hydroxyl is a comparable hydrogen-bond acceptor as compared to water, as the first solvation-shell structure of $g(r_{HO^*})$ is almost identical to that of $g(r_{HO})$. In contrast, for the LRC-ωPBE+D3 simulation, •OH is slightly less active as a hydrogen-bond acceptor (in comparison to a water molecule), as here the first maximum in $g(r_{HO^*})$ is peaked at a larger value of r and is much less intense as compared to $g(r_{HO})$. Comparing the two simulations, one can say that the distribution of O–H···O* hydrogen bonds is much less structured in the LRC-ωPBE+D3 simulation.

It is worth noting that the more structured B3LYP+D3 results presented here for oxygen–hydrogen RDFs are generally in agreement with previous *ai*MD simulations using the GGA functional BLYP in small simulation cells.[8,9] In contrast, BLYP-SIC results[8] more closely resemble our LRC-ωPBE+D3 results. As noted above, this suggests a very subtle interplay between simulation size, self-interaction, and the fraction of exact exchange.

3.2 Counting hydrogen bonds

To further investigate the local solvation structure and hydrogen-bonding network around the radical, we quantify the number of water···hydroxyl hydrogen bonds at each time step by taking the nearest five water molecules to the •OH and using an angle-dependent distance cutoff,[99,100]

$$r_{cut}(\theta)/\text{Å} = -0.00044(\theta/\text{deg})^2 + 3.3, \quad (5)$$

to determine whether a hydrogen bond exists or not. Here, θ is the angle between the $\mathbf{r}_{OO}$ and $\mathbf{r}_{OH}$ vectors. For angles $\theta \leq 50^\circ$, we judge that a hydrogen bond exists if $r_{O^*O} \leq r_{cut}$. Histograms of the number of hydrogen bonds determined in this way are reported in Fig. 4. Fitted probability distributions are superimposed on each histogram. (Results for the three functionals are superimposed on one another in Fig. S12, ESI.†)

For both the B3LYP+D3 and PBE0+D3 simulations, the average number of hydrogen bonds in the first solvation shell is $\langle n \rangle = 3$, which is also the most probable number. Of these three hydrogen bonds, the one where the radical acts as the hydrogen donor is very stable during the dynamics. In the other two (more fluxional) hydrogen bonds, the O* acts as the acceptor. There is also a fourth water molecule that forms a hemibond with the •OH for more than half of the snapshots. To check whether this seemingly itinerant fourth water molecule might be an artifact of the cutoff criterion used in eqn (5), we increased the cutoff from 3.3 to 3.4 Å. This modification alters the (already small) number of structures with $n = 4$ hydrogen bonds by $<2\%$, suggesting that the distributions in Fig. 4 are reasonably stable with respect to the cutoff criterion.

The LRC-ωPBE+D3 results are somewhat different, with $n \approx 2$ hydrogen bonds on average but a broader distribution as compared to those observed using the global hybrid functionals. The H*-donor hydrogen bond persists in simulations with the range-separated hybrid, so the difference is approximately one fewer hydrogen bonds in which O* acts as an acceptor. Because the first solvation shell of •OH contains $\approx$4 water molecules, this means that two of these molecules remain uncoordinated to the radical, on average, although we observe intermittent structures where one of these forms a hemibond with the radical. Consistent with the RDFs discussed above, this counting of the hydrogen bonds suggests that the local solvation environment around •OH is less structured in the case of LRC-ωPBE+D3 than it is for either PBE0+D3 or B3LYP+D3 and in fact the former closely resembles results obtained by VandeVondele and Sprik using the BLYP-SIC functional.[8] In contrast, the distribution of hydrogen bonds obtained from the two global hybrid functionals closely matches with previously-reported BLYP results.[6–9]

3.3 Hemibond formation

Given the differences in local solvation structure obtained using different functionals, we next examine some correlated joint probability distributions between geometric parameters, in an effort to provide some range of parameters that might characterize hemibonded structures. Chipman[30] has previously offered such suggestions, which are given in Fig. 1, but these were based on calculations for the binary HO•···H_2O complex and may not be fully transferable to the condensed phase. In Fig. 5 and 6, we examine correlations between the geometrical parameters r_{O^*O}, α, and χ (as defined in Fig. 1), in the form of two-dimensional joint probability distributions. (We use the water molecule closest to the radical in order to define these

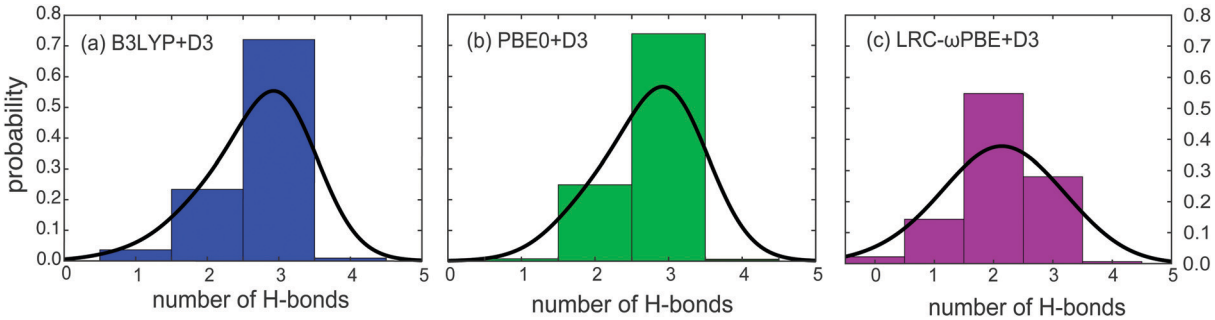

Fig. 4 Histograms for the number of hydrogen bonds to •OH, considering the nearest five water molecules to the radical, for simulations performed using (a) B3LYP+D3, (b) PBE0+D3, and (c) LRC-ωPBE+D3. Black curves are fits to the normalized probability distributions.

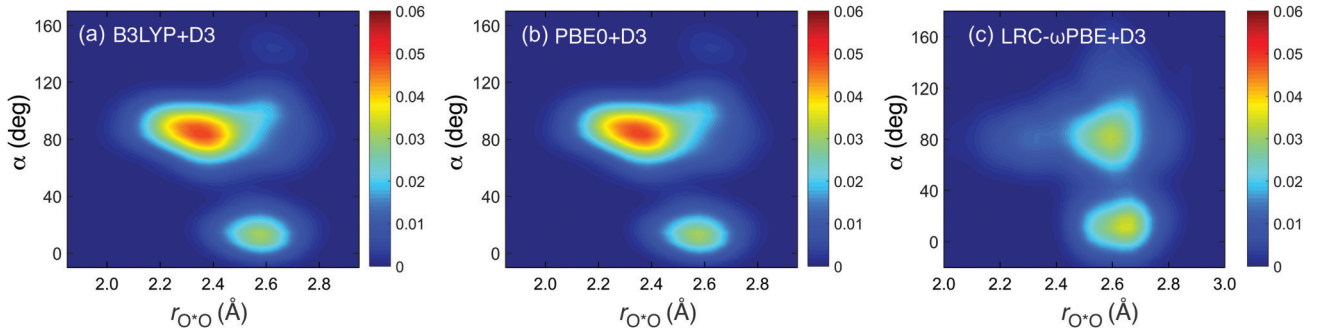

Fig. 5 Two-dimensional joint distributions of r_{O^*O} and α, for simulations using (a) B3LYP+D3, (b) PBE0+D3, and (c) LRC-ωPBE+D3. These geometrical parameters are defined in Fig. 1.

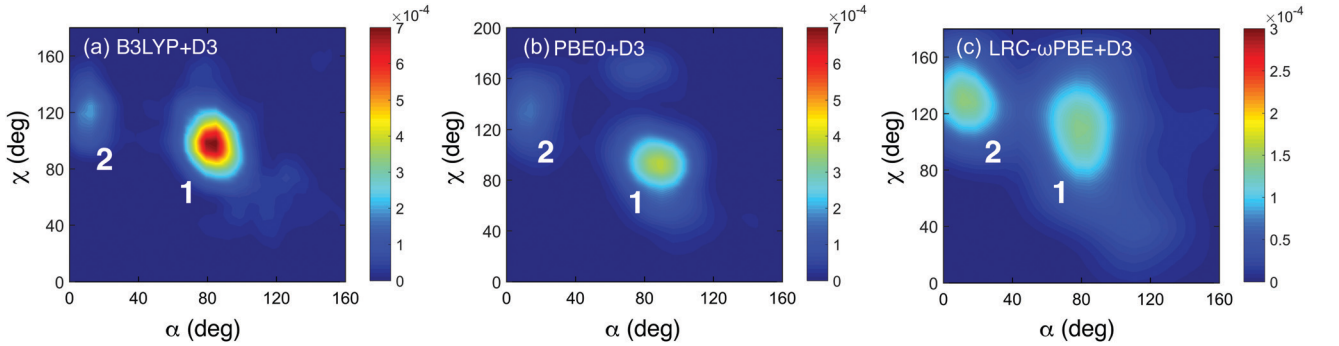

Fig. 6 Two-dimensional joint distributions of α and χ (as defined in Fig. 1), for simulations using (a) B3LYP+D3, (b) PBE0+D3, and (c) LRC-ωPBE +D3. The two prominent features are labeled "1" and "2" for convenient reference in the text.

parameters.) The distributions in Fig. 5 and 6 are based on 400–500 snapshots separated in time by 10 fs intervals.

Two-dimensional distributions in r_{O^*O} and α are shown in Fig. 5. A bimodal probability distribution is obtained for each of the three functionals that we examine in detail, which is similar for the B3LYP+D3 and PBE0+D3 functionals but somewhat different for LRC-ωPBE+D3. For the former, the most probable parameters are $r_{O^*O} \leq 2.5$ Å and $70^\circ \leq \alpha \leq 110^\circ$, which looks like the classic hemibond as suggested by Chipman[30] (see Fig. 1). The second feature in the probability distribution for these functionals appears between $r_{O^*O} = 2.5$ Å and $r_{O^*O} = 2.7$ Å, with $\alpha < 40^\circ$, and is characteristic of hydrogen bonding with $^\bullet$OH as the donor. The latter (hydrogen-bonded) feature remains roughly similar in simulations performed using LRC-ωPBE+D3, although the distribution of angles α is somewhat wider, consistent with a solvation environment that is less structured overall. The most significant difference relative to the B3LYP+D3 and PBE0+D3 simulations, however, occurs in the region $70^\circ \leq \alpha \leq 110^\circ$. Here, the probability distribution with $r_{O^*O} = 2.5$ Å is diminished almost to zero, consistent with the lack of any feature in $g(r_{O^*O})$ at smaller values of r_{O^*O} than the hydrogen-bonding peak. Moreover, regarding the joint (r_{O^*O},α) probability distribution in Fig. 5c, the boundary between the large- and small-α features in the distribution is not as sharp as it was in the case of B3LYP+D3 or PBE0+D3.

Joint distributions in (α,χ) are plotted in Fig. 6. Here, the distributions obtained using B3LYP+D3 and PBE0+D3 are weakly bimodal, with features that are labeled "1" and "2" in Fig. 6. The far more significant peak is feature 1, appearing in the region where $70^\circ \leq \alpha \leq 110^\circ$ and $70^\circ \leq \chi \leq 120^\circ$, whereas feature 2 is much fainter and is characterized by $\alpha < 30^\circ$ and $100^\circ \leq \chi \leq 130^\circ$. The latter is not a minor feature in the LRC-ωPBE+D3 simulations, however, but is comparable to feature 1. Based on Chipman's criteria for the hemibond (Fig. 1), it seems likely that feature 1 results predominantly from hemibonded configurations while feature 2 arises from hydrogen-bonded configurations. This is interesting in view of the fact that both features are prominent in the LRC-ωPBE+D3 simulation, whereas other considerations have pointed (perhaps) to less hemibonding in the solvation structure obtained using this functional. Comparison to the (r_{O^*O},α) distributions in Fig. 5 suggests that because feature 2 is characterized by $\alpha \leq 30^\circ$, it is also likely characterized by $r_{O^*O} > 2.5$ Å, making it difficult to ascribe hemibonding character to this feature in the (α,χ) distributions.

Based on analysis of the B3LYP+D3 and PBE0+D3 data, suitable geometric criteria for the hemibond appear to be $r_{O^*O} < 2.5$ Å, $70^\circ \leq \alpha \leq 110^\circ$, and $70^\circ \leq \chi \leq 120^\circ$, although the range for χ is a rougher estimate because some hydrogen-bonded water molecules do attach to $^\bullet$OH with similar values of χ. (One-dimensional probability distributions in χ do not exhibit any clear separation into hydrogen-bonded and hemibonded parts; see Fig. S15, ESI.†) However, the geometrical analysis attempted in this section has exposed some ambiguities,

especially concerning hemibonding in the LRC-ωPBE+D3 simulations. In an attempt to resolve these, and to formulate a cleaner definition of hemibonding, we next look for an electronic rather than a geometrical definition.

3.4 Spin charge distribution

VandeVondele and Sprik[8] showed that the distribution of spin charges (obtained *via* Mulliken analysis applied to the spin density $\rho_\alpha - \rho_\beta$) is useful to investigate hemibonding. Specifically, the sum s_{OH} of the spin charges on the O* and H* provides a measure of "spin leakage" (delocalization of the unpaired electron) onto the neighboring water molecules, as indicated by values $s_{OH} < 1$. We expect this leakage to be more pronounced for hemibonded structures with their characteristic three-electron bond. At the same time, artificial spin leakage is also a signature of SIE. In an attempt to use s_{OH} to obtain a consistent electronic definition of the hemibond, we will analyze all snapshots from the different simulations using a common density-functional approach, namely OT-LRC-ωPBE+D3, although we tune this functional separately for each simulation. (This will be discussed in detail in the context of the electronic spectroscopy, in Section 4.)

Histograms of s_{OH} from different trajectories are plotted in Fig. 7, normalized to unit area so that they may be interpreted as probability distributions. Each distribution is bimodal (albeit only weakly so in the LRC-ωPBE+D3 case), with one peak around 0.85e and the other around 0.95e (or 0.87e and 0.97e in the case of LRC-ωPBE+D3). We associate the first of these peaks, corresponding to greater spin leakage, with hemibonded configurations, which is confirmed by joint probability distributions in r_{O^*O} and s_{OH} (Fig. S17, ESI†), indicating that the distribution centered at the smaller value of s_{OH} is associated with $r_{O^*O} < 2.5$ Å, whereas the other feature, corresponding to the radical center being almost entirely localized on the •OH moiety, is primarily associated with r_{O^*O} = 2.5–2.7 Å. We note that the fraction of the snapshots corresponding to the hemibonded feature decreases in the order

$$\text{B3LYP+D3} > \text{PBE0+D3} > \text{LRC-}\omega\text{PBE+D3},$$

from ≈40% of the total for B3LYP+D3 to ≈10% for LRC-ωPBE+D3, suggesting the same trend for the relative population of the hemibonded species. Similar behavior is observed upon going from simulations with BLYP to those with BLYP-SIC.[8] For the LRC-ωPBE+D3 simulation, the joint probability distribution in (r_{O^*O},s_{OH}) is peaked strongly around r_{O^*O} = 2.65 Å and s_{OH} = 0.97e (see Fig. S17c, ESI†), with only a faint tail corresponding to smaller values of s_{OH} and shorter values of r_{O^*O}.

The question arises whether these hemibonded configurations constitute inherent structures,[101] or are instead fluctuations that are only accessed transiently, perhaps representing saddle points or unstable minima on the underlying potential energy surface. To address this, we took a few snapshots from the B3LYP+D3 and PBE0+D3 simulations and quenched them using a few hundred steps of QM/MM energy minimization with periodic boundary conditions. No significant change in the value of s_{OH} is observed over the course of the optimizations, as shown for several examples in Fig. S11 (ESI†). It therefore appears that the hemibond is indeed an inherent structure of •OH(aq), rather than an energetic saddle point that is accessed only fleetingly.

4 Electronic spectroscopy

4.1 Ensemble-averaged results

Based on EOM-CCSDT calculations performed on binary HO•···H_2O complexes, Chipman[30,70] has suggested that the feature around 5.4 eV (230 nm) in the absorption spectrum of •OH(aq) arises from a CT transition whose oscillator strength is ≈10× larger in hemibonded configurations than it is in hydrogen-bonded structures. This result was not affected in any meaningful way by the addition of a continuum solvation model.[70]

Here, we compute the absorption spectrum of •OH(aq) in full atomistic detail using TD-DFT. As described in Section 2.2, these calculations are carried out within a QM/MM formalism using four different functionals and the 6-31++G* basis set. Fig. 8 shows a comparison of the spectra thus obtained. Absorption maxima are listed in Table 3, which also provides the optimally-tuned range separation parameters for each functional. Spectra for different trajectory simulations are computed using the same set of functionals, but the LRC-ωPBE and LRC-μBLYP functionals are tuned separately for each

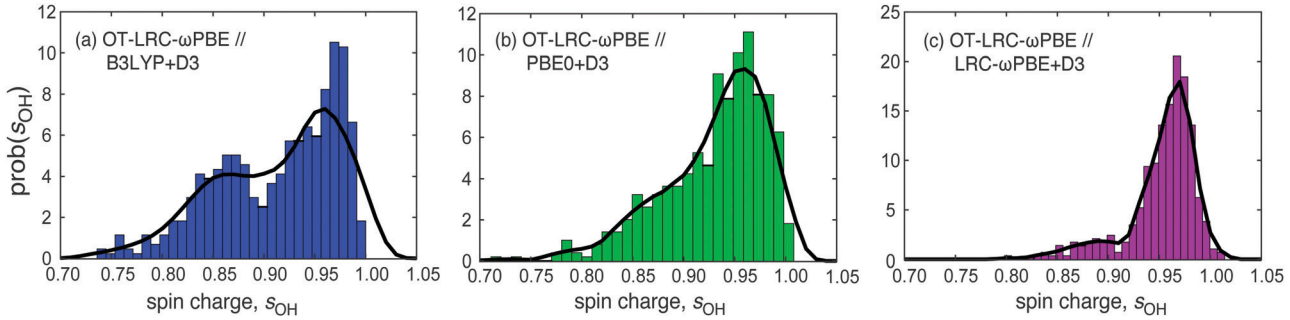

Fig. 7 Histograms for the total spin charge s_{OH} on the •OH moiety, for simulations performed using (a) B3LYP+D3, (b) PBE0+D3, and (c) LRC-ωPBE+D3. The spin charges are computed at the OT-LRC-ωPBE+D3/6-31+G* level, with ω tuned separately for each simulation. Black curves are fits to the distribution, which can be interpreted as probability distributions for s_{OH}.

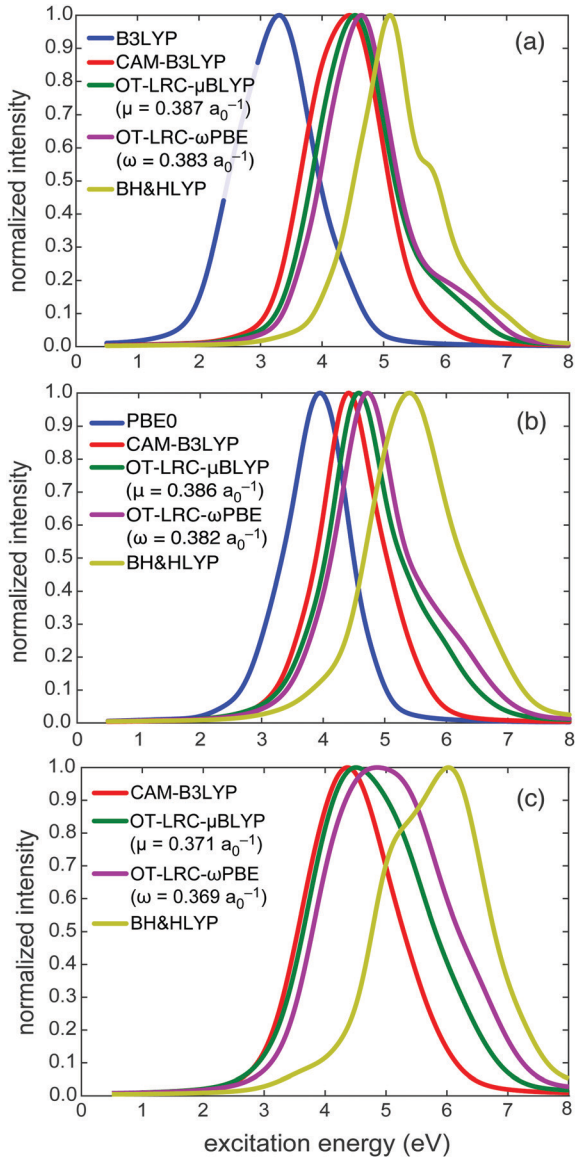

Fig. 8 Ensemble-averaged absorption spectra for •OH(aq) computed using TD-DFT with various functionals as indicated, for QM/MM trajectory data obtained from (a) B3LYP+D3, (b) PBE0+D3, or (c) LRC-ωPBE+D3 simulations.

simulation so that the condition in eqn (4) is satisfied in an average way for a given set of structural snapshots from the same simulation.

Spectra from the OT-LRC functionals exhibit absorption maxima of 4.5–4.8 eV, which represents a significant red-shift with respect to the experimental maximum at 5.4 eV.[71–74] Results with CAM-B3LYP are consistently $\approx$0.15 eV to the red of the OT-LRC results, although we do not place much significance on a shift of this magnitude, which is smaller than the intrinsic accuracy of TD-DFT even in favorable cases.[102] For the B3LYP+D3 and PBE0+D3 trajectories, we also performed TD-DFT calculations with the same functional that was used for the QM/MM simulation itself, and these results lie significantly to the red of the CAM-B3LYP spectrum, consistent with the appearance of spurious, low-energy states involving CT either to or from the solvent.[103–105]

Table 3 TD-DFT excitation energies (in eV) corresponding to the absorption maxima for •OH(aq) computed using various density functionals, for three different QM/MM trajectories. Footnotes indicate the range-separation parameters used in each case

TD-DFT Functional	Trajectory		
	B3LYP	PBE0	LRC-ωPBE[a]
B3LYP	3.285	—	—
PBE0	—	3.496	—
CAM-B3LYP	4.434	4.400	4.351
OT-LRC-μBLYP	4.540[b]	4.550[c]	4.502[d]
OT-LRC-ωPBE	4.644[e]	4.704[f]	4.877[g]
BH&HLYP	5.110	5.395	6.003

[a] ω = 0.380 a_0^{-1}. [b] μ = 0.387 a_0^{-1}. [c] μ = 0.386 a_0^{-1}. [d] μ = 0.371 a_0^{-1}. [e] ω = 0.383 a_0^{-1}. [f] ω = 0.382 a_0^{-1}. [g] ω = 0.369 a_0^{-1}.

In contrast to these results, all of which are red-shifted relative to experiment, the BH&HLYP functional predicts absorption at higher energies. In fact, TD-BH&HLYP spectra obtained from the PBE0+D3 and B3LYP+D3 trajectories are a good match to the experimental absorption maximum, as shown in Fig. S23 (ESI†). This is not altogether surprising given that TD-BH&HLYP was previously shown to match gas-phase EOM-CCSDT results for HO•$\cdots$H$_2$O.[30] For neat liquid water, TD-BH&HLYP calculations do a good job of describing the band shape of the UV spectrum, although the first peak is slightly blue-shifted (by $\approx$0.3 eV) in QM regions with $\leq$5 water molecules.[106] The shift is smaller and in the opposite direction (0.1–0.2 eV, to the red) when comparably small clusters are extracted from liquid simulations and TD-DFT calculations performed using the LRC-μBOP functional[96,97] with μ = 0.47 a_0^{-1}.[107,108] Thus, there is some precedent for the level of agreement with the •OH(aq) spectrum that is observed in the present calculations.

When applied to the LRC-ωPBE+D3 trajectory, however, TD-BH&HLYP calculations predict an absorption maximum $\approx$0.6 eV higher than experiment. To the extent that the favorable comparison between TD-BH&HLYP and EOM-CCSDT in binary complexes may be carried over to larger hydrated •OH models (and TD-BH&HLYP contains enough exact exchange to avoid many of the spurious CT problems exhibited by functionals such as B3LYP),[109] this overestimation of the absorption maximum for LRC-ωPBE+D3 configurations may point to a too-small role for hemibonded configurations in that particular simulation. This will become more evident when we decompose the absorption spectrum into contributions from hemibonded structures and non-hemibonded structures, in Section 4.2.

Whereas the spectra in Fig. 8 are normalized, for direct comparison to the vertical excitation spectra reported elsewhere, we present the ensemble-averaged oscillator strength distribution in Fig. S21 (ESI†), without normalization. For B3LYP and PBE0 the oscillator strength at the absorption maximum lies in the range 0.09–0.10, comparable to published results for HO•$\cdots$H$_2$O,[70] and 5–6$\times$ larger than the absolute oscillator strength computed for LRC-ωPBE at its absorption maximum. Given the enhanced oscillator strength that is

associated with transitions from hemibonded geometries,[30,70] this further suggests that hemibonded configurations are a minority population in the LRC-ωPBE+D3 trajectory, consistent with other evidence documented above.

Examining the nature of the transitions that are responsible for the $^{\bullet}$OH(aq) absorption spectrum, we find that the ones with largest oscillator strength are CT excitations, $1b_2(H_2O) \rightarrow 2p\pi(^{\bullet}OH)$. The donor orbital is the frontier lone pair of water and the acceptor is the SOMO of the radical, in a hemibonded arrangement. Analogous CT excitations from hydrogen-bonded water molecules do appear but with much smaller oscillator strengths. The lower absolute oscillator strength in the ensemble-averaged spectrum obtained from LRC-ωPBE+D3 trajectories (Fig. S21, ESI†) is therefore consistent with the appearance of fewer hemibonded configurations in that simulation, as compared to the B3LYP+D3 and PBE0+D3 simulations.

Finally, we note that the presence of a high-energy shoulder in some of the spectra in Fig. 8 hints at a higher-energy feature. Experimentally, an additional (weak) transition is observed at lower energy,[76] and is attributed to a localized transition on $^{\bullet}$OH that is the solution-phase analogue of the gas-phase $\tilde{A} \leftarrow \tilde{X}$ transition. In TD-DFT calculations of the kind reported here, however, where numerous explicit solvent molecules are included in addition to the chromophore, the oscillator strength is never converged on the high-energy side of the spectrum, due to the use of a finite number of excited states. In principle, this leading edge could be pushed to higher energy by computing additional excited states, but the relatively large number of water molecules in the QM region would make it prohibitively expensive to resolve and converge features at 6–7 eV above the ground state. Where broad-band spectra are required, a potentially cost-effective alternative is the "real-time" approach to TD-DFT,[110] but this requires careful consideration of boundary conditions for condensed-phase applications. In the present work, we have not attempted to push the spectra beyond what is shown in Fig. 8.

4.2 Spectral decompositions

The bimodal nature of the probability distributions for coordinates $r_{O^{\bullet}O}$ and α, and for the $^{\bullet}$OH spin charge s_{OH}, strongly suggests that the trajectories consist mainly of two types of structures, hemibonded and not hemibonded. This motivates us to attempt a decomposition of the simulated absorption spectra into contributions from each of these two populations, in order to test Chipman's idea that a minority population of hemibonded structures is primarily responsible for the absorption feature at 5.4 eV.[30]

Bimodal distributions of s_{OH} can be separated by setting a cutoff value around 0.90–0.92e (see Fig. 7), and $r_{O^{\bullet}O}$ distributions can be separated with a cutoff of $r_{O^{\bullet}O}$ = 2.5 Å (see Fig. 5). For an individual liquid configuration, we can estimate the absorption maximum E_{max} as a weighted average of vertical excitation energies,[111,112]

$$E_{max} = \frac{\sum_{i=1}^{n} f_{0i} E_i}{\sum_{j=1}^{n} f_{0j}}, \quad (6)$$

which allows us to construct joint distributions (s_{OH}, E_{max}) and ($r_{O^{\bullet}O}$, E_{max}). The former is depicted for the B3LYP+D3 simulation in Fig. 9, using the OT-LRC-ωPBE functional to compute n = 15 excited states. (Other distributions can be found in Fig. S18 and S19, ESI.†) Using this distribution, we can examine hypothetical scenarios in which the simulation is restricted to particular values of s_{OH}, and from Fig. 9 it is clear that the restriction $s_{OH} \leq 0.92e$ affords an absorption maximum $E_{max} \approx$ 4.7 eV. This is perfectly aligned with the absorption maximum computed with the same functional when averaged over all configurations; see Fig. 8a. The same is true for the PBE0+D3 simulation (see Fig. S18b, ESI†), but this analysis is more ambiguous for the LRC-ωPBE+D3 simulation (Fig. S18c, ESI†), because there are very few snapshots with $s_{OH} \leq 0.92e$.

That said, the largest oscillator strength obtained from individual snapshots exhibit correlations with the instantaneous value of s_{OH} that are obvious even for the LRC-ωPBE+D3 simulation. Joint distributions (s_{OH}, max$\{f_{0n}\}$) are plotted in Fig. 10, displaying these trends. Decreasing s_{OH}, which signals spin delocalization onto the water molecules (or in other words, candidate structures for hemibonding) clearly correlates with a larger values for the maximum oscillator strength. This is true even for the LRC-ωPBE+D3 simulation where the spin leakage is smallest.

In view of this trend, we applied a cutoff s_{OH} = 0.95e to snapshots from each trajectory, in order to partition each spectrum into contributions from hemibonded and non-hemibonded configurations. These decompositions are shown in Fig. 11. For the B3LYP+D3 and PBE0+D3 trajectories, 63% and 57% (respectively) of the snapshots have $s_{OH} \leq 0.95e$, but these configurations are responsible for essentially the entire absorption spectrum. For the LRC-ωPBE+D3 simulation only 33% of the configurations have $s_{OH} \leq 0.95e$, nevertheless this minority population contributes roughly equally to the spectral intensity alongside the 67% of snapshots for which there is little or no spin leakage.

A similar analysis can be applied using $r_{O^{\bullet}O}$ to partition the spectra, rather than s_{OH}, and indeed a joint distribution

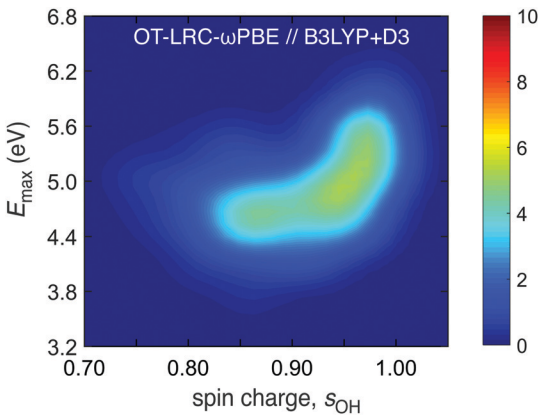

Fig. 9 Joint distribution of the spin charge on the hydroxyl moiety (s_{OH}) *versus* the absorption maximum E_{max}. Calculations were performed using the OT-LRC-ωPBE functional on geometries obtained from QM/MM simulations using B3LYP+D3.

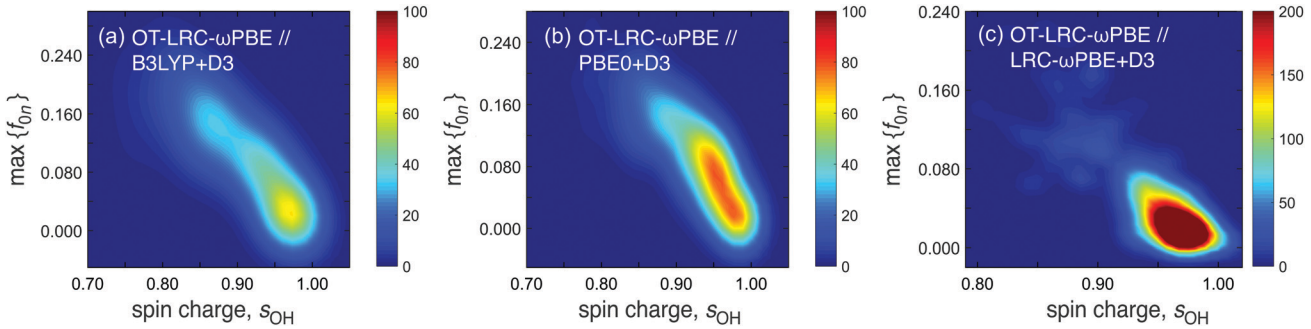

Fig. 10 Joint distribution of the spin charge on the hydroxyl moiety (s_{OH}) *versus* the largest oscillator strength (max{f_{0n}}), for QM/MM simulations performed using (a) B3LYP+D3, (b) PBE0+D3, and (c) LRC-ωPBE+D3.

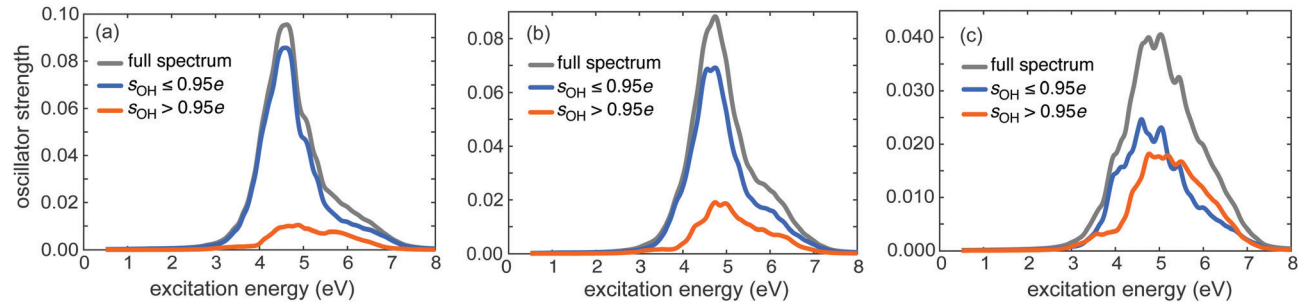

Fig. 11 TD-DFT absorption spectra computed using the OT-LRC-ωPBE functional and separated into two contributions according to the value of the spin charge on the hydroxyl moiety, s_{OH}. Results are shown for (a) the B3LYP+D3 trajectory, (b) the PBE0+D3 trajectory, and (c) the LRC-ωPBE+D3 trajectory.

($r_{O^{\bullet}O}$, s_{OH}) shows strong correlation between the two as shown in Fig. S17 (ESI†). Snapshots with $r_{O^{\bullet}O} \leq 2.5$ Å are generally associated with $s_{OH} \leq 0.95e$, and restricting the averaging to only those snapshots with $r_{O^{\bullet}O} \leq 2.5$ Å retains approximately the same absorption maximum as unrestricted averaging (Fig. S19, ESI†). Spectral decompositions, according to whether $r_{O^{\bullet}O}$ is greater than or less than 2.5 Å, are shown in Fig. S24 (ESI†) and the results of this partition closely resemble what is shown in Fig. 11. Specifically, for the two global hybrid functionals, nearly the entirety of the oscillator strength is carried by configurations with $r_{O^{\bullet}O} \leq 2.5$ Å, whereas for the LRC-ωPBE+D3 simulation this is a minority population but is still responsible for approximately half of the integrated oscillator strength.

5 Conclusions

We have reported on QM/MM simulations of $^{\bullet}$OH(aq) using various hybrid and range-separated hybrid functionals. Hemibonded structures of the radical appear as one of the main solvation motifs for simulations using B3LYP+D3 or PBE0+D3, as indicated by oxygen–oxygen RDFs and by analysis of the spin density, which is more delocalized in hemibonded configurations. This is a different conclusion than was reached in recent *ai*MD simulations of $^{\bullet}$OH(aq) using the same functionals,[21] where no hemibonded configurations are reported at all. The theoretical framework is somewhat different in the present work, nevertheless this disparity remains a subject for further investigation.

For QM/MM simulations using LRC-ωPBE+D3, hemibonded configurations are significantly suppressed but not absent. Shorter trajectories at the BLYP+D3, BH&HLYP+D3, and HF+D3 levels of theory highlight the profound impact of exact exchange on the structure of the solvated radical. Simulations using the GGA functional BLYP+D3 exhibit a pronounced shoulder in $g(r_{O^{\bullet}O})$ at small values of $r_{O^{\bullet}O}$, a feature that has long been taken as the signature of a hemibond.[8] This feature is present, albeit less pronounced, in the B3LYP+D3 and PBE0+D3 trajectories but is absent for other functionals considered here. Even for trajectories where this feature is absent, however, we nevertheless observe a strong correlation between oscillator strengths computed for the low-energy excited states and the spin charge s_{OH} on the $^{\bullet}$OH moiety. This suggests that in all of the simulations, ''spin leakage'' (delocalization) onto the water molecules is associated with enhanced absorption at UV wavelengths.

Ensemble-averaged absorption spectra of $^{\bullet}$OH(aq) were computed from the aforementioned trajectories using a variety of TD-DFT approaches. Notably, TD-BH&HLYP calculations have previously been shown to afford good agreement with benchmark transition energies for the binary $HO^{\bullet}\cdots H_2O$ complex.[30] In the present work, this functional affords the best agreement with the experimental absorption maximum when

the underlying solvent configurations are taken from simulations using the B3LYP+D3 and PBE0+D3 functionals. In contrast, TD-BH&HLYP calculations overestimate the experimental absorption maximum by $\approx$0.6 eV when applied to the LRC-ωPBE+D3 trajectory, suggesting that the paucity of hemibonded structures in the latter leads to an artificial blue-shift in the spectrum.

Chipman[30] has suggested that the absorption band of $^{\bullet}$OH(aq) at 230 nm (5.4 eV), which is strongly blue-shifted from the absorption maximum of gas-phase $^{\bullet}$OH (at 307 nm or 4.0 eV), is a result of solvent-to-radical CT bands whose oscillator strengths are quite large compared to those for excitations localized on the radical, with the radical-localized transitions of $^{\bullet}$OH(aq) closer to the gas-phase absorption energy. In the present work, we evaluated this hypothesis by partitioning the ensemble-averaged spectra in several ways, according to thresholds applied to either the spin charge s_{OH}, which affords an electronic definition of the hemibond, or else to the distance $r_{O^{\bullet}O}$, which provides a geometric definition. By either definition, nearly the entire oscillator strength of the spectrum simulated using either B3LYP+D3 or PBE0+D3 trajectories is carried by hemibonded configurations of the radical. For the LRC-ωPBE+D3 simulations, such configurations represent a minority species but are still responsible for approximately half of the integrated oscillator strength.

The hypothesis put forward by Chipman therefore appears to be on very solid footing, despite lingering questions regarding the prevalence of the hydroxyl-water hemibond. Whereas optical spectroscopy following pulse radiolysis has been used to identify sulfur–sulfur hemibonds in solution-phase cation radicals,[36–39] the situation is more complicated when the radical in question is a byproduct of solvent radiolysis. Our analysis suggests that the UV spectrum of $^{\bullet}$OH(aq) is insufficient to differentiate between various DFT-based simulations that predict a persistent and pervasive hemibonded motif, *versus* those where the hemibond is a minor population. It is unclear what other experimental observable might be able to differentiate between these cases. Resonance Raman spectroscopy might be a possibility, insofar as the radical exhibits an electronic transition that is isolated from the neat solvent, while vibrational spectroscopy has recently been used to identify sulfur–sulfur hemibonds in $(H_2S)_n^+$ clusters[32,33] and $(CH_3SH)_2^+$.[35] In the aqueous phase, resonance Raman experiments were instrumental in identifying the solvation motif of e^-(aq).[29,88,113]

On the theoretical side, further work is necessary to ascertain whether the hemibond is a self-interaction artifact (as has long been the conventional wisdom),[8] or whether finite-size effects may affect this conclusion (as has recently been demonstrated).[12] A third possibility is that a delicate interplay between these two effects can alter the structure of $^{\bullet}$OH(aq); indeed, the present simulations suggest that the energetics of the hemibond are sensitive to both factors, and that the true physical structure of the aqueous radical may lie near an inflection point in the space of simulation parameters. In that case, relatively minor modifications to the computational protocol might manifest as dramatically different predictions for the solvation structure. This is not without precedent for an aqueous radical.[29,114–116] Additional simulations are planned to address this issue.

Conflicts of interest

J. M. H. serves on the board of directors of Q-Chem, Inc.

Acknowledgements

This work was supported by National Science Foundation grant no. CHE-1665322 and CHE-1955282. Calculations were performed at the Ohio Supercomputer Center under project PAA-0003.[117]

Notes and references

1 B. C. Garrett, D. A. Dixon, D. M. Camaioni, D. M. Chipman, M. A. Johnson, C. D. Jonah, G. A. Kimmel, J. H. Miller, T. N. Rescigno, P. J. Rossky, S. S. Xantheas, S. D. Colson, A. H. Laufer, D. Ray, P. F. Barbara, D. M. Bartels, K. H. Becker, K. H. Bowen, Jr., S. E. Bradforth, I. Carmichael, J. V. Coe, L. R. Corrales, J. P. Cowin, M. Dupuis, K. B. Eisenthal, J. A. Franz, M. S. Gutowski, K. D. Jordan, B. D. Kay, J. A. LaVerne, S. V. Lymar, T. E. Madey, C. W. McCurdy, D. Meisel, S. Mukamel, A. R. Nilsson, T. M. Orlando, N. G. Petrik, S. M. Pimblott, J. R. Rustad, G. K. Schenter, S. J. Singer, A. Tokmakoff, L.-S. Wang, C. Wittig and T. S. Zwier, Role of water in electron-initiated processes and radical chemistry: Issues and scientific advances, *Chem. Rev.*, 2005, **105**, 355–389.

2 H. Herrmann, D. Hoffmann, T. Schaefer, P. Bräuer and A. Tilgner, Tropospheric aqueous-phase free-radical chemistry: Radical sources, spectra, reaction kinetics and prediction tools, *Comput. Phys. Commun.*, 2010, **11**, 3796–3822.

3 I. S. A. Isaksen and S. B. Dalsøren, Getting a better estimate of an atmospheric radical, *Science*, 2011, **331**, 38–39.

4 B. Lipinski, Hydroxyl radical and its scavengers in health and disease, *Oxid. Med. Cell. Longev.*, 2011, **2011**, 1–9.

5 S. Gligorovski, R. Strekowski, S. Barbati and D. Vione, Environmental implications of hydroxyl radicals ($^{\bullet}$OH), *Chem. Rev.*, 2015, **115**, 13051–13092. Erratum: *Chem. Rev.*, 2018, **118**, 2296.

6 P. Vassilev, M. J. Louwerse and E. J. Baerends, Ab initio molecular dynamics simulation of the OH$^{\bullet}$ radical in liquid water, *Chem. Phys. Lett.*, 2004, **398**, 212–216.

7 P. Vassilev, M. J. Louwerse and E. J. Baerends, Hydroxyl radical and hydroxide ion in liquid water: A comparative electron density functional study, *J. Phys. Chem. B*, 2005, **109**, 23605–23610.

8 J. VandeVondele and M. Sprik, A molecular dynamics study of the hydroxyl radical in solution applying self-interaction-corrected density functional methods, *Phys. Chem. Chem. Phys.*, 2005, **7**, 1363–1367.

9 J. M. Khalack and A. P. Lyubartsev, Solvation structure of hydroxyl radical by Car-Parrinello molecular dynamics, *J. Phys. Chem. A*, 2005, **109**, 378–386.
10 I. M. Svishchev and A. Y. Plugatyr, Hydroxyl radical in aqueous solution: Computer simulation, *J. Phys. Chem. B*, 2005, **109**, 4123–4128.
11 R. D'Auria, I.-F. W. Kuo and D. J. Tobias, Ab initio molecular dynamics simulation of the $OH^{\bullet}$ radical in liquid water, *J. Phys. Chem. A*, 2008, **112**, 4644–4650.
12 E. Codorniu-Hernández and P. G. Kusalik, Insights into the solvation and mobility of the hydroxyl radical in aqueous solution, *J. Chem. Theory Comput.*, 2011, **7**, 3725–3732.
13 E. Codorniu-Hernández and P. G. Kusalik, Mobility mechanism of hydroxyl radicals in aqueous solution via hydrogen transfer, *J. Am. Chem. Soc.*, 2012, **134**, 532–538.
14 E. Codorniu-Hernández and P. G. Kusalik, Hydroxyl radicals in ice: Insights into local structure and dynamics, *Phys. Chem. Chem. Phys.*, 2012, **14**, 11639–11650.
15 E. Codorniu-Hernández, A. D. Boese and P. G. Kusalik, The hemibond as an alternative condensed phase structure for the hydroxyl radical, *Can. J. Chem.*, 2013, **91**, 544–551.
16 G. F. von Rudorff, R. Jakobsen, K. M. Rosso and J. Blumberger, Improving the performance of hybrid functional-based molecular dynamics simulation through screening of Hartree-Fock exchange forces, *J. Chem. Theory Comput.*, 2017, **13**, 2178–2184.
17 A. Pabis, J. Szala-Bilnik and D. Swiatla-Wojcik, Molecular dynamics study of the hydration of the hydroxyl radical at body temperature, *Phys. Chem. Chem. Phys.*, 2011, **13**, 9458–9468.
18 J. Szala-Bilnik and D. Swiatla-Wojcik, Hydration of OH radical in high temperature water, *J. Mol. Liq.*, 2011, **164**, 34–38.
19 D. Swiatla-Wojcik and J. Szala-Bilnik, Mechanism of OH radical hydration: A comparative computational study of liquid and supercritical solvent, *J. Chem. Phys.*, 2012, **136**, 064510.
20 A. Genova, D. Ceresoli and M. Pavanello, Avoiding fractional electrons in subsystem DFT based *ab-initio* molecular dynamics yields accurate models for liquid water and solvated OH radical, *J. Chem. Phys.*, 2016, **144**, 234105.
21 C. Apostolidou, OH radical in water from *ab initio* molecular dynamics simulation employing hybrid functionals, *J. Chem. Phys.*, 2019, **151**, 064111.
22 L. Kjellsson, K. D. Nanda, J.-E. Rubensson, G. Doumy, S. H. Southworthh, P. J. Ho, A. M. March, A. Al Haddad, Y. Kumagai, M.-F. Tu, R. D. Schaller, T. Debnath, M. S. Bin Mohd Yusof, C. Arnold, W. F. Schlotter, S. Moeller, G. Coslovich, J. D. Koralek, M. P. Minitti, M. L. Vidal, M. Simon, R. Santra, Z.-H. Loh, S. Coriani, A. I. Krylov and L. Young, Resonant inelastic x-ray scatternig reveals hidden local transitions of the aqueous OH radical, *Phys. Rev. Lett.*, 2020, **124**, 236001.
23 G. V. Buxton, C. L. Greenstock, W. P. Helman and A. B. Ross, Critical review of rate constants for reactions of hydrated electrons, hydrogen atoms and hydroxyl radicals ($^{\bullet}OH/^{\bullet}O$) in aqueous solution, *J. Phys. Chem. Ref. Data*, 1988, **17**, 513–886.
24 A. J. Elliot, D. R. McCracken, G. V. Buxton and N. D. Wood, Estimation of rate constants for near-diffusion-controlled reactions in water at high temperatures, *J. Chem. Soc., Faraday Trans.*, 1990, **86**, 1539–1547.
25 M. Holz, S. R. Heil and A. Sacco, Temperature-dependent self-diffusion coefficients of water and six selected molecular liquids for calibration in accurate ^{1}H NMR PFG measurements, *Phys. Chem. Chem. Phys.*, 2000, **2**, 4740–4742.
26 N. Agmon, The Grotthuss mechanism, *Chem. Phys. Lett.*, 1995, **244**, 456–462.
27 N. Agmon, Mechanism of hydroxide mobility, *Chem. Phys. Lett.*, 2000, **319**, 247–252.
28 D. Marx, A. Chandra and M. E. Tuckerman, Aqueous basic solutions: Hydroxide solvation, structural diffusion, and comparison to the hydrated proton, *Chem. Rev.*, 2010, **110**, 2174–2216.
29 J. M. Herbert, Structure of the aqueous electron, *Phys. Chem. Chem. Phys.*, 2019, **21**, 20538–20565.
30 D. M. Chipman, Hemibonding between hydroxyl radical and water, *J. Phys. Chem. A*, 2011, **115**, 1161–1171.
31 T. Drewello, C. B. Lebrilla, H. Schwarz, L. J. de Koning, R. H. Fokkens, N. M. M. Nibbering, E. Anklam and K.-D. Asmus, Formation of a two-centre, three-electron, sulphur-sulphur bond in the gas phase, *J. Chem. Soc., Chem. Commun.*, 1987, 1381–1383.
32 D. Wang and A. Fujii, Spectroscopic observation of two-center three-electron bonded (hemi-bonded) structures of $(H_2S)_n^+$ clusters in the gas phase, *Chem. Sci.*, 2017, **8**, 2667–2670. Erratum: *Chem. Sci.*, 2018, **9**, 2893–3894.
33 D. Wang, K. Hattori and A. Fujii, The S$\therefore\pi$ hemibond and its competition with the S$\therefore$S hemibond in the simplest model system: Infrared spectroscopy of the [benzene-$(H_2S)_n]^+$ (n = 1-4) radical cation clusters, *Chem. Sci.*, 2019, **10**, 7260–7268.
34 A. J. Illies, P. Livant and M. L. McKee, Association of dimethyl sulfide radical cation with dimethyl sulfide. Strength of a two-center three-electron bond, *J. Am. Chem. Soc.*, 1988, **110**, 7980–7984.
35 M. Xie, Z. Shen, D. Wang, A. Fujii and Y.-P. Lee, Spectral characterization of three-electron two-center (3e-2c) bonds of gaseous $CH_3\therefore S(H)CH_3$ and $(CH_3SH)_2^+$ and enhancement of the 3e–2c bond upon protonation, *J. Phys. Chem. Lett.*, 2018, **9**, 3725–3730.
36 K.-D. Asmus, Stabilization of oxidized sulfur centers in organic sulfides. Radical cations and odd-electron sulfur–sulfur bonds, *Acc. Chem. Res.*, 1979, **12**, 436–442.
37 S. A. Chaudhri and K.-D. Asmus, Experimental evidence of the $[H_2SSH_2]^+$ radical cation in solution, *Angew. Chem., Int. Ed. Engl.*, 1981, **20**, 672–673.
38 J. Mönig, R. Goslich and K.-D. Asmus, Thermodynamics of S$\therefore$S $2\sigma/1\sigma^*$ three-electron bonds and deprotonation kinetics of thioether radical cations in aqueous solution, *Ber. Bunsenges. Phys. Chem.*, 1986, **90**, 115–121.
39 K.-D. Asmus, Sulfur-centered three-electron bonded radical species, in *Sulfur-Centered Reactive Intermediates in Chemistry and Biology*, ed. C. Chatgilialoglu and K.-D. Asmus, Vol. 197

of NATO Advanced Science Institute Series A: Life Sciences, Plenum Press, New York, 1990, pp. 155–172.
40 A. J. Cohen, P. Mori-Sanchez and W. Yang, Challenges for density functional theory, *Chem. Rev.*, 2012, **112**, 289–320.
41 B. Brada, P. C. Hiberty and A. Savin, A systematic failing of current density functionals: Overestimation of two-center three-electron bonding energies, *J. Phys. Chem. A*, 1998, **102**, 7872–7877.
42 J. Gräfenstein, E. Kraka and D. Cremer, Effect of the self-interaction error for three-electron bonds: On the development of new exchange-correlation functionals, *Phys. Chem. Chem. Phys.*, 2004, **6**, 1096–1112.
43 P. Zawadzki, J. Rossmeisl and K. W. Jacobsen, Electronic hole transfer in rutile and anatase TiO_2: Effect of a delocalization error in the density functional theory on the charge transfer barrier height, *Phys. Rev. B: Condens. Matter Mater. Phys.*, 2011, **84**, 121203(R).
44 G. Pacchioni, F. Frigoli, D. Ricci and J. A. Weil, Theoretical description of hole localization in a quartz Al center: The importance of exact electron exchange, *Phys. Rev. B: Condens. Matter Mater. Phys.*, 2000, **63**, 054102.
45 J. Lægsgaard and K. Stokbro, Hole trapping at Al impurities in silica: A challenge for density functional theories, *Phys. Rev. Lett.*, 2001, **86**, 2834–2837.
46 M. d'Avezac, M. Calandra and F. Mauri, Density functional theory description of hole-trapping in SiO_2: A self-interaction-corrected approach, *Phys. Rev. B: Condens. Matter Mater. Phys.*, 2005, **71**, 205210.
47 M. Sodupe, J. Bertran, L. Rodríguez-Santiago and E. J. Baerends, Ground state of the $(H_2O)_2^+$ radical cation: DFT versus post-Hartree-Fock methods, *J. Phys. Chem. A*, 1999, **103**, 166–170.
48 E. Livshits, R. S. Granot and R. Baer, A density functional theory for studying ionization processes in water clusters, *J. Phys. Chem. A*, 2011, **115**, 5735–5744.
49 Y. A. Mantz, F. L. Gervasio, T. Laino and M. Parrinello, Charge localization in stacked radical cation DNA base pairs and the benzene dimer studied by self-interaction corrected density-functional theory, *J. Phys. Chem. A*, 2007, **111**, 105–112.
50 J. M. Herbert and M. Head-Gordon, Calculation of electron detachment energies for water cluster anions: An appraisal of electronic structure methods, with application to $(H_2O)_{20}^-$ and $(H_2O)_{24}^-$, *J. Phys. Chem. A*, 2005, **109**, 5217–5229.
51 J. M. Herbert, The quantum chemistry of loosely-bound electrons, in *Reviews in Computational Chemistry*, ed. A. L. Parill and K. Lipkowitz, Wiley-VCH, 2015, ch. 8, vol. 28, pp. 391–517.
52 T. Frigato, J. VandeVondele, B. Schmidt, C. Schütte and P. Jungwirth, Ab initio molecular dynamics simulation of a medium-sized water cluster anion: From an interior to a surface-located excess electron via a delocalized state, *J. Phys. Chem. A*, 2008, **112**, 6125–6133.
53 P. R. Tentscher and J. S. Arey, Binding in radical-solvent binary complexes: Benchmark energies and performance of approximate methods, *J. Chem. Theory Comput.*, 2013, **9**, 1568–1579.
54 E. R. Johnson, M. Salamone, M. Bietti and G. A. DiLabio, Modeling noncovalent radical-molecule interactions using conventional density-functional theory: Beware erroneous charge transfer, *J. Phys. Chem. A*, 2013, **117**, 947–952.
55 M.-C. Kim, E. Sim and K. Burke, Ions in solution: Density corrected density functional theory (DC-DFT), *J. Chem. Phys.*, 2014, **140**, 18A528.
56 M.-C. Kim, H. Park, S. Son, E. Sim and K. Burke, Improved DFT potential energy surfaces via improved densities, *J. Phys. Chem. Lett.*, 2015, **6**, 3802–3807.
57 A. D. Becke, Density-functional exchange-energy approximation with correct asymptotic behavior, *Phys. Rev. A: At., Mol., Opt. Phys.*, 1988, **38**, 3098–3100.
58 C. Lee, W. Yang and R. G. Parr, Development of the Colle-Salvetti correlation-energy formula into a functional of the electron density, *Phys. Rev. B: Condens. Matter Mater. Phys.*, 1988, **37**, 785–789.
59 A. D. Boese, N. L. Doltsinis, N. C. Handy and M. Sprik, New generalized gradient approximation functionals, *J. Chem. Phys.*, 2000, **112**, 1670–1678.
60 C. Adamo and V. Barone, Toward reliable density functional methods without adjustable parameters: The PBE0 model, *J. Chem. Phys.*, 1999, **110**, 6158–6170.
61 O. A. Vydrov and G. E. Scuseria, Effect of the Perdew-Zunger self-interaction correction on the thermochemical performance of approximate density functionals, *J. Chem. Phys.*, 2004, **121**, 8187–8193.
62 D. R. Lonsdale and L. Goerigk, The one-electron self-interaction error in 74 density functional approximations: A case study on hydrogenic mono- and dinuclear systems, *Phys. Chem. Chem. Phys.*, 2020, **22**, 15805–15830.
63 D. Rappoport, N. R. M. Crawford, F. Furche and K. Burke, Approximate density functionals: Which should I choose?, in *Encyclopedia of Inorganic Chemistry*, ed. R. B. King, R. H. Crabtree, C. M. Lukehart, D. A. Atwood and R. A. Scott, Wiley, 2006.
64 J. L. Bao, L. Gagliardi and D. G. Truhlar, Self-interaction error in density functional theory: An appraisal, *J. Phys. Chem. Lett.*, 2018, **9**, 2353–2358.
65 A. D. Becke, Density-functional thermochemistry. III. The role of exact exchange, *J. Chem. Phys.*, 1993, **98**, 5648–5652.
66 J. Heyd, G. E. Scuseria and M. Ernzerhof, Hybrid functionals based on a screened Coulomb potential, *J. Chem. Phys.*, 2003, **118**, 8207–8215. Erratum: *J. Chem. Phys.*, 2006, **124**, 219906.
67 S. Grimme, J. Antony, S. Ehrlich and H. Krieg, A consistent and accurate *ab initio* parameterization of density functional dispersion correction (DFT-D) for the 94 elements H-Pu, *J. Chem. Phys.*, 2010, **132**, 154104.
68 O. Oldenberg and F. F. Rieke, Kinetics of OH radicals as determined by their absorption spectrum III. A quantitative test for free OH; probabilities of transition, *J. Chem. Phys.*, 1938, **6**, 439–447.

69 S. Pellerin, J. M. Cormier, F. Richard, K. Musiol and J. Chapelle, A spectroscopic diagnostic method using UV OH band spectrum, *J. Phys. D: Appl. Phys.*, 1996, **29**, 726.
70 D. M. Chipman, Absorption spectrum of OH radical in water, *J. Phys. Chem. A*, 2008, **112**, 13372–13381.
71 J. K. Thomas, J. Rabani, M. S. Matheson, E. J. Hart and S. Gordon, Absorption spectrum of the hydroxyl radical, *J. Phys. Chem.*, 1966, **70**, 2409–2410.
72 P. Pagsberg, H. Christensen, J. Rabani, G. Nilsson, J. Fenger and S. O. Nielsen, Far-ultraviolet spectra of hydrogen and hydroxyl radicals from pulse radiolysis of aqueous solutions. direct measurement of the rate of H + H, *J. Phys. Chem.*, 1969, **73**, 1029–1038.
73 A. Treinin and E. Hayon, Charge transfer spectra of halogen atoms in water. correlation of the electronic transition energies of iodine, bromine, chlorine, hydroxyl, and hydrogen radicals with their electron affinities, *J. Am. Chem. Soc.*, 1975, **97**, 1716–1721.
74 G. Czapski and B. H. J. Bielski, Absorption spectra of the $^{\bullet}$OH and $O^{\bullet-}$ radicals in aqueous solutions, *Radiat. Phys. Chem.*, 1993, **41**, 503–505.
75 S. O. Nielsen, B. D. Michael and E. J. Hart, Ultraviolet absorption spectra of e_{aq}^{-}, H, OH, D, and OD from pulse radiolysis of aqueous solutions, *J. Phys. Chem.*, 1976, **80**, 2482–2488.
76 I. Janik, D. M. Bartels and C. D. Jonah, Hydroxyl radical self-recombination reaction and absorption spectrum in water up to 350 °C, *J. Phys. Chem. A*, 2007, **111**, 1835–1843.
77 M.-K. Tsai, K. Kowalski, M. Valiev and M. Dupuis, Signature OH absorption spectrum from cluster models of solvation: A solvent-to-solute charge transfer state, *J. Phys. Chem. A*, 2007, **111**, 10478–10482.
78 M. Yamaguchi, Hemibonding of hydroxyl radical and halide anion in aqueous solution, *J. Phys. Chem. A*, 2011, **115**, 14620–14628.
79 G. J. Hoffman, P. K. Gurunathan, J. S. Francisco and L. V. Slipchenko, Excited states of OH-$(H_2O)_n$ clusters for n = 1–4: An *ab initio* study, *J. Chem. Phys.*, 2014, **141**, 104315.
80 M. A. Rohrdanz, K. M. Martins and J. M. Herbert, A long-range-corrected density functional that performs well for both ground-state properties and time-dependent density functional theory excitation energies, including charge-transfer excited states, *J. Chem. Phys.*, 2009, **130**, 054112.
81 Y. Shao, Z. Gan, E. Epifanovsky, A. T. B. Gilbert, M. Wormit, J. Kussmann, A. W. Lange, A. Behn, J. Deng, X. Feng, D. Ghosh, M. Goldey, P. R. Horn, L. D. Jacobson, I. Kaliman, R. Z. Khaliullin, T. Kús, A. Landau, J. Liu, E. I. Proynov, Y. M. Rhee, R. M. Richard, M. A. Rohrdanz, R. P. Steele, E. J. Sundstrom, H. L. Woodcock III, P. M. Zimmerman, D. Zuev, B. Albrecht, E. Alguire, B. Austin, G. J. O. Beran, Y. A. Bernard, E. Berquist, K. Brandhorst, K. B. Bravaya, S. T. Brown, D. Casanova, C.-M. Chang, Y. Chen, S. H. Chien, K. D. Closser, D. L. Crittenden, M. Diedenhofen, R. A. DiStasio Jr., H. Do, A. D. Dutoi, R. G. Edgar, S. Fatehi, L. Fusti-Molnar, A. Ghysels, A. Golubeva-Zadorozhnaya, J. Gomes, M. W. D. Hanson-Heine, P. H. P. Harbach, A. W. Hauser, E. G. Hohenstein, Z. C. Holden, T.-C. Jagau, H. Ji, B. Kaduk, K. Khistyaev, J. Kim, J. Kim, R. A. King, P. Klunzinger, D. Kosenkov, T. Kowalczyk, C. M. Krauter, K. U. Lao, A. Laurent, K. V. Lawler, S. V. Levchenko, C. Y. Lin, F. Liu, E. Livshits, R. C. Lochan, A. Luenser, P. Manohar, S. F. Manzer, S.-P. Mao, N. Mardirossian, A. V. Marenich, S. A. Maurer, N. J. Mayhall, C. M. Oana, R. Olivares-Amaya, D. P. O'Neill, J. A. Parkhill, T. M. Perrine, R. Peverati, P. A. Pieniazek, A. Prociuk, D. R. Rehn, E. Rosta, N. J. Russ, N. Sergueev, S. M. Sharada, S. Sharma, D. W. Small, A. Sodt, T. Stein, D. Stück, Y.-C. Su, A. J. W. Thom, T. Tsuchimochi, L. Vogt, O. Vydrov, T. Wang, M. A. Watson, J. Wenzel, A. White, C. F. Williams, V. Vanovschi, S. Yeganeh, S. R. Yost, Z.-Q. You, I. Y. Zhang, X. Zhang, Y. Zhao, B. R. Brooks, G. K. L. Chan, D. M. Chipman, C. J. Cramer, W. A. Goddard III, M. S. Gordon, W. J. Hehre, A. Klamt, H. F. Schaefer III, M. W. Schmidt, C. D. Sherrill, D. G. Truhlar, A. Warshel, X. Xu, A. Aspuru-Guzik, R. Baer, A. T. Bell, N. A. Besley, J.-D. Chai, A. Dreuw, B. D. Dunietz, T. R. Furlani, S. R. Gwaltney, C.-P. Hsu, Y. Jung, J. Kong, D. S. Lambrecht, W. Liang, C. Ochsenfeld, V. A. Rassolov, L. V. Slipchenko, J. E. Subotnik, T. Van Voorhis, J. M. Herbert, A. I. Krylov, P. M. W. Gill and M. Head-Gordon, Advances in molecular quantum chemistry contained in the Q-Chem 4 program package, *Mol. Phys.*, 2015, **113**, 184–215.
82 R. Baer, E. Livshits and U. Salzner, Tuned range-separated hybrids in density functional theory, *Annu. Rev. Phys. Chem.*, 2010, **61**, 85–109.
83 W. L. Jorgensen, J. Chandrasekhar, J. D. Madura, R. W. Imprey and M. L. Klein, Comparison of simple potential functions for simulating liquid water, *J. Chem. Phys.*, 1983, **79**, 926–935.
84 P. H. Hünenberger, Thermostat algorithms for molecular dynamics simulations, *Adv. Polym. Sci.*, 2005, **173**, 105–149.
85 J. M. Herbert and M. Head-Gordon, Accelerated, energy-conserving Born-Oppenheimer molecular dynamics *via* Fock matrix extrapolation, *Phys. Chem. Chem. Phys.*, 2005, **7**, 3269–3275.
86 Z. C. Holden, R. M. Richard and J. M. Herbert, Periodic boundary conditions for QM/MM calculations: Ewald summation for extended Gaussian basis sets, *J. Chem. Phys.*, 2013, **139**, 244108. Erratum: *J. Chem. Phys.*, 2015, **142**, 059901.
87 Z. C. Holden, B. Rana and J. M. Herbert, Analytic energy gradients for the QM/MM-Ewald method using atomic charges derived from the electrostatic potential: Theory, implementation, and application to *ab initio* molecular dynamics of the aqueous electron, *J. Chem. Phys.*, 2019, **150**, 144115.
88 S. Dasgupta, B. Rana and J. M. Herbert, *Ab initio* investigation of the resonance Raman spectrum of the hydrated electron, *J. Phys. Chem. B*, 2019, **123**, 8074–8084.
89 C. M. Breneman and K. B. Wiberg, Determining atom-centered monopoles from molecular electrostatic potentials. The need for high sampling density in formamide conformational analysis, *J. Comput. Chem.*, 1990, **11**, 361–373.

90 M. M. Francl and L. E. Chirlian, The pluses and minuses of mapping atomic charges to electrostatic potentials, in *Reviews in Computational Chemistry*, ed. K. B. Lipkowitz and D. B. Boyd, Wiley-VCH, New York, 2000, ch. 1, vol. 14, pp. 1–32.

91 J. M. Herbert, L. D. Jacobson, K. U. Lao and M. A. Rohrdanz, Rapid computation of intermolecular interactions in molecular and ionic clusters: Self-consistent polarization plus symmetry-adapted perturbation theory, *Phys. Chem. Chem. Phys.*, 2012, **14**, 7679–7699.

92 M. Zheng and M. P. Waller, Adaptive quantum mechanics/molecular mechanics methods, *Wiley Interdiscip. Rev.: Comput. Mol. Sci.*, 2016, **6**, 369–385.

93 C. N. Rowley and B. Roux, The solvation structure of Na^+ and K^+ in liquid water determined from high level *ab initio* molecular dynamics simulations, *J. Chem. Theory Comput.*, 2012, **8**, 3526–3535.

94 S. Hirata and M. Head-Gordon, Time-dependent density functional theory within the Tamm-Dancoff approximation, *Chem. Phys. Lett.*, 1999, **314**, 291–299.

95 T. Yanai, D. P. Tew and N. C. Handy, A new hybrid exchange-correlation functional using the Coulomb-attenuating method (CAM-B3LYP), *Chem. Phys. Lett.*, 2004, **393**, 51–57.

96 M. A. Rohrdanz and J. M. Herbert, Simultaneous benchmarking of ground- and excited-state properties with long-range-corrected density functional theory, *J. Chem. Phys.*, 2008, **129**, 034107.

97 R. M. Richard and J. M. Herbert, Time-dependent density-functional description of the ^1L_a state in polycyclic aromatic hydrocarbons: Charge-transfer character in disguise?, *J. Chem. Theory Comput.*, 2011, **7**, 1296–1306.

98 B. Alam, A. F. Morrison and J. M. Herbert, Charge separation and charge transfer in low-lying excited states of pentacene, *J. Phys. Chem. C*, 2020, **124**, 24653–24666.

99 L. D. Jacobson and J. M. Herbert, A one-electron model for the aqueous electron that includes many-body electron-water polarization: Bulk equilibrium structure, vertical electron binding energy, and optical absorption spectrum, *J. Chem. Phys.*, 2010, **133**, 154506.

100 S. Laricchia, E. Fabiano, L. Constantin and F. D. Sala, Generalized gradient approximations of the noninteracting kinetic energy from the semiclassical atom theory: Rationalization of the accuracy of the frozen density embedding theory for nonbonded interactions, *J. Chem. Theory Comput.*, 2011, **7**, 2439–2451.

101 F. H. Stillinger, *Energy Landscapes, Inherent Structures, and Condensed-Matter Phenomena*, Princeton University Press, Princeton, NJ, 2016.

102 A. D. Laurent and D. Jacquemin, TD-DFT benchmarks: A review, *Int. J. Quantum Chem.*, 2013, **113**, 2019–2039.

103 A. Lange and J. M. Herbert, Simple methods to reduce charge-transfer contamination in time-dependent density-functional calculations of clusters and liquids, *J. Chem. Theory Comput.*, 2007, **3**, 1680–1690.

104 A. W. Lange, M. A. Rohrdanz and J. M. Herbert, Charge-transfer excited states in a π-stacked adenine dimer, as predicted using long-range-corrected time-dependent density functional theory, *J. Phys. Chem. B*, 2008, **112**, 6304–6308. Erratum: *J. Phys. Chem. B*, 2008, **112**, 7345.

105 J. M. Herbert, X. Zhang, A. F. Morrison and J. Liu, Beyond time-dependent density functional theory using only single excitations: Methods for computational studies of excited states in complex systems, *Acc. Chem. Res.*, 2016, **49**, 931–941.

106 R. A. Mata, B. J. C. Cabral, C. Millot, K. Coutinho and S. Canuto, Dynamic polarizability, Cauchy moments, and the optical spectrum of liquid water: A sequential molecular dynamics quantum mechanical approach, *J. Chem. Phys.*, 2009, **130**, 014505.

107 P. C. do Couto and D. M. Chipman, Insights into the ultraviolet spectrum of liquid water from model calculations, *J. Chem. Phys.*, 2010, **132**, 244307.

108 P. C. do Couto and D. M. Chipman, Insights into the ultraviolet spectrum of liquid water from model calculations: The different roles of donor and acceptor hydrogen bonds in water pentamers, *J. Chem. Phys.*, 2012, **137**, 184301.

109 R. J. Magyar and S. Tretiak, Dependence of spurious charge-transfer excited states on orbital exchange in TDDFT: Large molecules and clusters, *J. Chem. Theory Comput.*, 2007, **3**, 976–987.

110 Y. Zhu and J. M. Herbert, Self-consistent predictor/corrector algorithms for stable and efficient integration of the time-dependent Kohn-Sham equation, *J. Chem. Phys.*, 2018, **148**, 044117.

111 L. D. Jacobson and J. M. Herbert, Theoretical characterization of four distinct isomer types in hydrated-electron clusters, and proposed assignments for photoelectron spectra of water cluster anions, *J. Am. Chem. Soc.*, 2011, **133**, 19889–19899.

112 F. Uhlig, J. M. Herbert, M. P. Coons and P. Jungwirth, Optical spectroscopy of the bulk and interfacial hydrated electron from ab initio calculations, *J. Phys. Chem. A*, 2014, **118**, 7507–7515.

113 M. J. Tauber and R. A. Mathies, Structure of the aqueous solvated electron from resonance Raman spectroscopy: Lessons from isotopic mixtures, *J. Am. Chem. Soc.*, 2003, **125**, 1394–1402.

114 L. Turi and A. Madarász, Comment on ''Does the hydrated electron occupy a cavity?'', *Science*, 2011, **331**, 1387.

115 L. D. Jacobson and J. M. Herbert, Comment on ''Does the hydrated electron occupy a cavity?'', *Science*, 2011, **331**, 1387.

116 J. M. Herbert and L. D. Jacobson, Structure of the aqueous electron: Assessment of one-electron pseudopotential models in comparison to experimental data and time-dependent density functional theory, *J. Phys. Chem. A*, 2011, **115**, 14470–14483.

117 Ohio Supercomputer Center, http://osc.edu/ark:/19495/f5s1ph73.

